



Recent advances in the study of the $\text{UO}_2\text{--PuO}_2$ phase diagram at high temperatures



R. Böhler^a, M.J. Welland^{a,1}, D. Prieur^a, P. Cakir^a, T. Vitova^b, T. Pruessmann^b, I. Pidchenko^b, C. Hennig^c, C. Guéneau^d, R.J.M. Konings^a, D. Manara^{a,*}

^a European Commission, Joint Research Centre, Institute for Transuranium Elements (ITU), P.O. Box 2340, 76125 Karlsruhe, Germany

^b Karlsruhe Institute of Technology, Institute for Nuclear Waste Management (INE), D-76125 Karlsruhe, Germany

^c Forschungszentrum Dresden-Rossendorf, Institute for Radiochemistry, D-01314 Dresden, Germany

^d Commissariat à l'Energie Atomique (CEA) Saclay – DEN/DANS/DPC/SCP/LM2T, 91191 Gif-sur-Yvette Cedex, France

ARTICLE INFO

Article history:

Received 2 December 2013

Accepted 17 February 2014

Available online 22 February 2014

ABSTRACT

Recently, novel container-less laser heating experimental data have been published on the melting behaviour of pure PuO_2 and PuO_2 -rich compositions in the uranium dioxide–plutonium dioxide system. Such data showed that previous data obtained by more traditional furnace heating techniques were affected by extensive interaction between the sample and its containment. It is therefore paramount to check whether data so far used by nuclear engineers for the uranium-rich side of the pseudo-binary dioxide system can be confirmed or not. In the present work, new data are presented both in the UO_2 -rich part of the phase diagram, most interesting for the uranium–plutonium dioxide based nuclear fuel safety, and in the PuO_2 side. The new results confirm earlier furnace heating data in the uranium-dioxide rich part of the phase diagram, and more recent laser-heating data in the plutonium-dioxide side of the system. As a consequence, it is also confirmed that a minimum melting point must exist in the $\text{UO}_2\text{--PuO}_2$ system, at a composition between $x(\text{PuO}_2) = 0.4$ and $x(\text{PuO}_2) = 0.7$ and $2900 \text{ K} \leq T \leq 3000 \text{ K}$. Taking into account that, especially at high temperature, oxygen chemistry has an effect on the reported phase boundary uncertainties, the current results should be projected in the ternary U–Pu–O system. This aspect has been extensively studied here by X-ray diffraction and X-ray absorption spectroscopy. The current results suggest that uncertainty bands related to oxygen behaviour in the equilibria between condensed phases and gas should not significantly affect the qualitative trend of the current solid–liquid phase boundaries.

© 2014 The Authors. Published by Elsevier B.V. Open access under [CC BY](https://creativecommons.org/licenses/by/4.0/) license.

1. Introduction

High temperature phase relationships (and particularly the melting behaviour) in the ternary U–Pu–O system have been thoroughly re-assessed in the last few years with the help of the CALPHAD thermodynamic optimisation approach taking into account the novel experimental data obtained at JRC-ITU by fast laser heating under quasi-containerless conditions and controlled atmosphere [1]. Some of these data displayed a considerable disagreement with respect to the existing literature, such as the melting behaviour of hyper-stoichiometric UO_{2+x} [2], pure PuO_2 [3], and Pu-rich $\text{UO}_2\text{--PuO}_2$ mixed oxides [4,5]. Data reported in earlier literature were obtained by “traditional” furnace heating

in a tungsten [6,7] (or, sometimes, rhenium [7,8]) crucible. The large differences with respect to the new JRC-ITU data have been explained on the basis of the elevated oxygen potential [9–12]:

$$\Delta G_{\text{O}_2}^{\text{AnO}_2} = \bar{\mu}_{\text{O}_2}^{\text{AnO}_2} = RT \ln a_{\text{O}_2}^{\text{AnO}_2}. \quad (1)$$

In Eq. (1), $\bar{\mu}_{\text{O}_2}^{\text{AnO}_2}$ is the oxygen chemical potential in a generic actinide dioxide (AnO_2), defined as the partial molar Gibbs free energy difference (ΔG_{O_2}) between a molecule of oxygen in its free (gaseous) state and the same oxygen in the dioxide AnO_2 . R is the ideal gas constant, T the absolute temperature, and $a_{\text{O}_2}^{\text{AnO}_2}$ the oxygen activity in the dioxide AnO_2 . This latter is defined as the product of the oxygen partial pressure (expressed in atm) by an activity coefficient (generally very close to 1) taking into account non-ideal interactions [11]. A high oxygen potential leads to an oxygen-driven high reactivity of the investigated compounds towards the metallic containment. This would affect most of the furnace results for the very high temperature behaviour of compounds displaying a high $\bar{\mu}_{\text{O}_2}$. For example, this assumption is confirmed by the fact that

* Corresponding author.

E-mail address: dario.manara@ec.europa.eu (D. Manara).

¹ Current address: Argonne National Laboratory (ANL), 9700 S. Cass Avenue, Argonne, IL 60439, USA.

melting/freezing points of actinide oxides obtained by the quasi-containerless laser heating approach agree less with furnace results, the higher the oxygen potential of the investigated compound (Fig. 1). For compounds with low oxygen potential (such as ThO₂ and stoichiometric UO₂), the agreement is good.

The (U, Pu)O₂ pseudo-binary section of the ternary U–Pu–O system is most interesting for nuclear applications, as mixed uranium–plutonium dioxides (MOX) constitute the main components of the nuclear fuel in many of the currently operational plants. In mixed oxides, it can be assumed that the oxygen potential evolves linearly from one to the other end member, e.g.:

$$\bar{\mu}_{O_2}^{MOX} = x(UO_2) \cdot \bar{\mu}_{O_2}^{UO_2} + x(PuO_2) \cdot \bar{\mu}_{O_2}^{PuO_2}. \quad (2)$$

Eq. (2) uses the same notation as Eq. (1), $x(AnO_2)$ representing the molar fraction of the compound AnO₂ (here An = U, Pu, and $x(UO_2) + x(PuO_2) = 1$). It can then be expected that the melting behaviour observed by quasi-containerless laser heating of mixed oxides richer in a high- $\bar{\mu}_{O_2}$ end member (PuO₂ in the (U, Pu)O₂ system) differs from that observed by traditional furnace heating, whereas a better agreement should be expected for the compositions richer in the low- $\bar{\mu}_{O_2}$ end member (UO₂ in the MOX case).

The present paper reports the main results of an experimental investigation performed at JRC-ITU by laser heating on the whole UO₂–PuO₂ system, in order to check the validity of the above reasoning. Particular attention has been devoted to compositions with $0 \leq x(PuO_2) \leq 0.5$, the range of interest for the uranium–plutonium dioxide based nuclear fuel currently used in most reactors.

The main concrete application of this work consists of checking whether data so far used by nuclear engineers for the uranium-rich side of the pseudo-binary dioxide system can be confirmed, since the melting behaviour of pure PuO₂ and PuO₂-rich compositions has been re-assessed in the last few years.

Possible segregation effects during fast heating and cooling across the melting transition have been studied on the whole UO₂–PuO₂ range with the help of powder X-ray diffraction (XRD), Raman spectroscopy (RS), X-ray absorption near-edge spectroscopy (XANES) and high-energy resolution XANES (HR-XANES). In addition, Phase Field modelling of the current laser heating experiments has helped the interpretation of the empirical thermograms.

2. Experimental and modelling approach

2.1. Sample preparation

A series of mixed (U, Pu)O₂ samples with plutonium dioxide molar fraction $x(PuO_2) = 0.037, 0.09, 0.25, 0.40, 0.50, 0.80, 0.90$

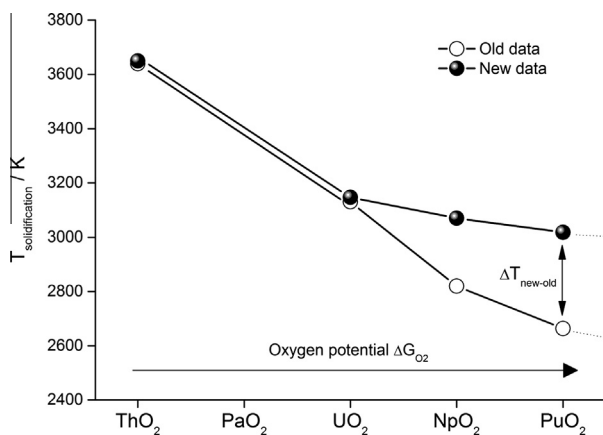


Fig. 1. The melting/solidification data measured by fast quasi-containerless laser heating in the actinide dioxide series compared with previous furnace heating data [8].

were prepared, calcinated, sintered and annealed according to the procedure reported in [4]. The different samples were designated with the label MOX and the amount-of-substance fraction $x(PuO_2) \cdot 100$. For example, MOX 9 signifies a MOX sample with $x(PuO_2) = 0.09$. Depleted uranium with an average mass fraction $w(^{238}U) = 0.9962\%$ was used for the sample fabrication, starting from dioxide powders or from a uranyl nitrate solution. The isotopic composition of the plutonium in the starting plutonium dioxide powders, determined by thermal ionisation mass spectrometry, was found to be $w(^{239}Pu) = 0.9354$ and $w(^{240}Pu) = 0.0632$, the remainder being ^{238}Pu , ^{241}Pu , ^{242}Pu and ^{241}Am isotopes, with mass fractions less than 0.01 each.

2.2. Laser heating and fast pyrometry setup

Details of the laser-heating setup used in this research have been reported in previous publications [1–4], although the technique has been partially improved in the present work.

Thermograms were measured by sub-millisecond resolution pyrometry on MOX samples laser heated beyond melting by a TRUMPF® Nd:YAG cw laser radiating at 1064.5 nm. Its power vs. time profile is programmable with a resolution of 1 ms. Pulses of different duration (100–1000 ms) and maximal power (180–675 W) were repeated on a 5 mm diameter spot on a single sample surface as well as on different samples of the same composition in order to obtain statistically significant datasets for each composition.

During the shots, the investigated MOX specimen was held in a sealed autoclave under controlled atmosphere. The atmosphere was chosen on the basis of thermodynamic equilibrium calculations between the condensed phases and the vapour [4], in order to maintain as much as possible the original composition of each sample throughout the heating/cooling cycles. Thus UO₂-rich samples were heated under an inert atmosphere (slightly pressurised argon at 0.3 MPa), whereas PuO₂-rich ones were preferably studied under dry compressed air (also at 0.3 MPa), in order to minimise oxygen losses from the condensed phases.

Excessive thermal shocks were minimised by starting each series of laser pulses from a pre-set temperature of about 1500 K. Each series consisted of three heating–cooling pulses on the same sample spot without cooling the material below an intermediate temperature of approximately 1500 K. The peak intensity and duration of the high-power pulses were increased from one heating–cooling cycle to the other, in order to check the result repeatability under slightly different experimental conditions (Fig. 2). This approach constituted a step forward in the laser heating technique. It ensured a better mechanical stability of the samples, on which several successive shots could be repeated to check the result reproducibility and the eventual effects of non-congruent vaporisation or segregation phenomena. The onset of melting was detected by the appearance of vibrations in the signal of a probe laser (Ar⁺ cw 750 mW to 1.5 W) reflected by the sample surface (reflected Light Signal technique, or RLS) [1]. The sample cooled naturally when the laser beam was switched off during the thermal cycle. Thermal arrests corresponding to solidification were then observed on the thermograms recorded by the fast pyrometers. These operate in the visible–near infrared range between 488 nm and 900 nm. The reference pyrometer wavelength was here 655 nm. This was calibrated according to the procedure already reported elsewhere [1–4]. The normal spectral emissivities of urania and plutonia have both been assumed to be equal to 0.83 as determined from previous work employing the same multi-wavelength pyrometry approach [2,3].

Uncertainty of the measurements was calculated according to the error propagation law [1], taking into account the uncertainty associated to pyrometer calibration, the emissivity, transmittance of the optical system and the accuracy in detecting the onset of

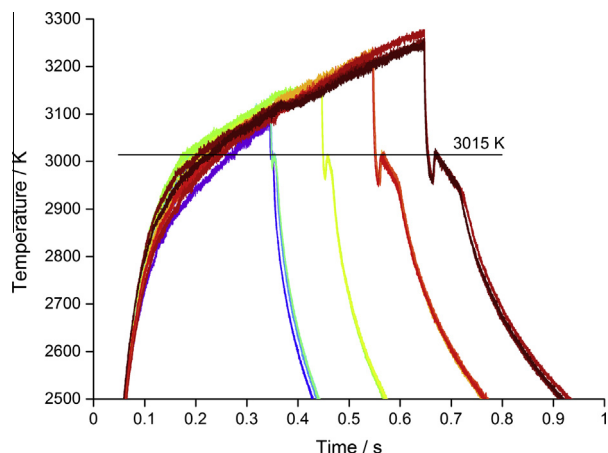


Fig. 2. Experimental thermograms recorded on a single MOX25 ($U_{0.75}Pu_{0.25}O_2$) sample over successive laser heating cycles. In each cycle, the sample surface was hit by three high-power laser pulses (starting at 0 s) separated by dwelling periods of several seconds during which it was kept at an intermediate temperature around 1500 K in order to minimise thermal shocks. The solidification temperature at 3015 K is suggested by the horizontal line.

vibrations in the RLS signal. The estimated cumulative uncertainty is thus lower than $\pm 2\%$ of the reported temperatures in the worst cases, with a 2- k coverage factor (corresponding to two standard deviation around the average value).

2.3. Pre- and post-melting material characterisation

Detailed characterisation of the material composition and structure and its evolution after laser heating/melting has been an essential part of this work. The main techniques employed to this goal are: PXRD, Raman spectroscopy and XANES.

2.3.1. Powder X-ray diffraction

PXRD analyses were performed with a Bruker[®] D8 Advance diffractometer (Cu $K\alpha_1$ radiation) with a 2θ range of 10–120° using 0.009° steps with 2 s of integration time per step at operating conditions of 40 kV and 40 mA.

Rietveld analysis of the recorded XRD patterns was performed with the help of the FullProf[®] software.

2.3.2. Raman spectroscopy

Raman spectra were measured with a Jobin-Yvon[®] T64000 spectrometer used in the single spectrograph configuration. Used excitation sources were the 488 nm and 514 nm lines of an Ar⁺ Coherent[®] laser, as well as the 647 nm and the 752 nm lines of a Kr⁺ Coherent[®] laser. Eventual polarisation effects on the Raman spectra were neglected in the present investigation. Actual wavelength and power were chosen at each measurement in order to optimise the signal/noise ratio (by minimising the material fluorescence) and reducing undesirable oxidation/burning effects on the sample surface. Moreover, the comparison of Raman spectra measured at different wavelengths permitted the identification of the vibrational or electronic origin of the peaks observed. Spectra were measured in a confocal microscope with a 50-fold magnification and long focal distance. This feature yielded a good spectral resolution ($\pm 1 \text{ cm}^{-1}$) independently of the surface roughness, with a spatial resolution of $2 \mu\text{m} \times 2 \mu\text{m}$. The spectrometer detector angle was calibrated daily with the T_{2g} excitation of a silicon single crystal, set at 520.5 cm^{-1} [13].

2.3.3. XANES spectroscopy

XANES and HR-XANES [14] measurements have been performed on approximately 4 mg of powdered sample mixed with 55 mg of boron nitride (BN). The data have been collected at the INE-Beamline, Angströmquelle Karlsruhe (ANKA) synchrotron radiation facility in Karlsruhe (Germany) [15] and at the ROBL-Beamline of the European Synchrotron Radiation Facility (ESRF) situated in Grenoble (France) [16].

MOX9 and MOX25 have been measured at the INE beamline with a Ge [422] double-crystal monochromator coupled to collimating and focusing Rh-coated mirrors. XANES spectra were collected at room temperature in transmission mode at the U L_{III} and at the Pu L_{III} edges.

U L_{III} -edge HR-XANES spectra of MOX9 were measured with a multi-analyser crystals Johann type spectrometer (MAC-spectrometer). Fluorescence emitted from U references and MOX9 and MOX9 m samples was diffracted by the 5 Ge(777) analyser crystals and focused on a SDD VORTEX. Sample, crystals and detector were positioned on a Rowland circle in the vertical plane with diameter of 1 m equal to the bending radius of the spherically bent analyser crystals. The MAC-Spectrometer was set at the maximum of the U $L\alpha_1$ emission line (13614 eV, 77.4° Bragg angle), whereas the incident energy was scanned to obtain U L_{III} edge (17166 eV) HR-XANES spectra. It was not possible to measure the experimental energy resolution at this photon energy due to the low elastic scattering cross section.

MOX3, MOX40 and MOX50 spectra were collected at ROBL using a double crystal monochromator mounted with Si (111) crystal coupled to collimating and focusing Rh coated mirrors. A 13-element Ge solid-state detector using a XIA (X-ray Instrumentation Associates) digital amplifier was used to acquire the fluorescence signal of the MOX3 at the Pu L_{III} edge.

The experimental XANES data were fitted within -20 eV and $+30 \text{ eV}$ compared to the E_0 position.

The energy calibration was accomplished by measuring simultaneously the K edge XANES spectra of a Y (17038 eV) and a Zr (17998 eV) foil for U L_{III} and Pu L_{III} , respectively. ATHENA software was used to remove the background and normalize the spectra [17]. The XANES spectra were compared with spectra of $UO_{2.00}$, $U(IV/V)_4O_9$, $U(V/VI)_3O_8$, PuO_2 and PuO_{2-x} reference compounds. The absorption edge (E_0) values were defined as the first inflexion point of the XANES spectra and set to the energy position of the first node of the second derivative. The energy position E_{WL} of the most intense absorption resonance (white-line, WL) maximum was found by determining the energy position of the first node of the first derivative. During both experimental runs at ANKA and at ESRF, XANES spectra of UO_2 , $U(IV/V)_4O_9$, $U(V/VI)_3O_8$, PuO_2 and $Pu(III/IV)O_{2-x}$ reference materials were collected. For the uranium references, commercial UO_2 was employed, whereas U_4O_9 and U_3O_8 were obtained by controlled oxidation in air at varying temperature and cross-checked by XRD. The PuO_2 reference sample was heat treated in an oxygen flux at 1400 K for 8 h in order to ensure a composition as close as possible to the O/Pu = 2.00 stoichiometry. The stoichiometry of the PuO_{2-x} reference, annealed in Ar + 6% H_2 for 8 h at 1900 K, was checked by Thermo-Gravimetric Analysis [4] and XRD measurements, yielding a O/Pu molar ratio of 1.88 ± 0.07 . This large uncertainty affecting the hypo-stoichiometric plutonium dioxide reference composition constituted one of the most limiting error sources in the current XANES analysis. The differences between the white line energy positions of these five compounds are in fair agreement with previous work [18–23]. Despite the use of similar Y and Zr calibration foils, a slight shift was observed between the UO_2 and PuO_2 white line energy positions collected at ESRF and at ANKA (see Table 2). However, as similar relative shifts were observed between the reference materials for both beam lines, a qualitative comparison of the data remains possible.

Table 1

Melting points detected by RLS and solidification points observed by thermal arrest analysis in this work on (U, Pu)O₂ samples. The Raman T_{2g} peak positions observed for each sample are reported, too.

x(PuO ₂) in MOX	No. of samples/shots	Melting Temp. (K)	2-σ Uncertainty band (K)	T _{2g} position (cm ⁻¹)	Solidification Temp. (K)	2-σ Uncertainty band (K)	T _{2g} position (cm ⁻¹)
0	2/15	n/a	n/a	447	3126	55.1	444.8
0.037	3/17	3129	65.4	447.5	3107	56.0	445.0
0.09	3/9	3116	70.2	443.8	3097	60.8	444.0
0.25	3/28	3052	63.6	456.0	3015	55.5	452.4
0.4	6/41	3015	55.8	464.1	2993	52.7	464.9
0.5	2/11	3007	52.8	466.8	2985	51.3	463.9
0.8	1/7	3023	54.6	474.2	3023	52.1	474.7
0.9	1/12	3037	60.2	475.2	3012	51.0	476.2
1	1/6	3040	59.9	477.3	3050	55.1	477.9

n/a = not available.

Table 2

Energy of the white line positions E_{WL} at the U L_{III} and Pu L_{III} edges.

	U L _{III} edge				Pu L _{III} edge			
	ANKA		ESRF		ANKA		ESRF	
	E _{WL} (eV)	ΔE _{WL} (eV)	E _{WL} (eV)	ΔE _{WL} (eV)	E _{WL} (eV)	ΔE _{WL} (eV)	E _{WL} (eV)	ΔE _{WL} (eV)
<i>Reference samples</i>								
UO ₂	17176.5	0	17174.8	0	–	–	–	–
U ₄ O ₉	17177.7	1.2	17175.8	1	–	–	–	–
U ₃ O ₈	17180.9	4.4	17178.9	4.1	–	–	–	–
PuO ₂	–	–	–	–	18068.1	0	18067.4	0
PuO _{2-x}	–	–	–	–	18067.6	–0.5	18066.9	–0.5
<i>Samples</i>								
UO ₂ m	n.m.	–	17174.9	0.1	n.m.	–	–	–
MOX 3	n.m.	–	17174.9	0.1	n.m.	–	18067.3	–0.1
MOX 3m	n.m.	–	17175	0.2	n.m.	–	18067.2	–0.2
MOX 9	17176.7	0.2	n.m.	–	n.d.	–	n.m.	–
MOX 9m	17176.6	0.1	n.m.	–	n.d.	–	n.m.	–
MOX 25	17176.6	0.1	n.m.	–	18068	–0.1	n.m.	–
MOX 25m	17176.7	0.2	n.m.	–	18067.9	–0.2	n.m.	–
MOX 40	n.m.	–	17175.1	0.3	n.m.	–	18067.1	–0.3
MOX 40m	n.m.	–	17175	0.2	n.m.	–	18067.3	–0.1
MOX 50m	n.m.	–	17175	0.2	n.m.	–	18067.2	–0.2
PuO ₂ m	n.m.	–	n.m.	–	n.m.	–	18067.1	–0.3

Notes: n.m.: not measured; n.d.: not detected, the noise to signal ratio of the XANES fluorescence spectrum was too high; ΔE_{WL} is the difference between the E_{WL} of the sample and the E_{WL} of the UO₂, respectively, PuO₂, measured at the same beamline.

2.4. Phase-Field modelling

The sometimes complex features of the observed thermal arrests can be attributed to the dynamics of the melting/solidification process of the small liquid pool formed in the solid matrix. Such dynamics have been studied with the help of numerical simulations of the current experiments, based on a Phase-Field approach to the heat and mass diffusion across the phase boundaries. This model determines the thermal transport coupled with phase stability through a Phase-Field parameter which tightly links the process kinetics to equilibrium thermodynamic treatments of the material. Such a parameter is identified by a scalar state variable φ representing the fraction of the stable phase at each physical point of the system (e.g. $\varphi = 1$ for the liquid, $\varphi = 0$ for the solid, $\varphi \in (0, 1)$ for a coexistence of the two). This approach permits a versatile description of the system including representation of phase boundaries with diffuse interfaces, whereas its main drawback is large computational expense, resulting in long calculation times. The model's mathematical and numerical details have already been described elsewhere [24,25]. They have been implemented in the finite element method software COMSOL Multiphysics®.

Many of the material parameters required as input for the model are unknown, especially at the very high temperatures encountered at the liquid state. Missing parameters were therefore

extrapolated from lower temperatures or taken from databases of pure UO₂ [2,26] when no other information was available. A first approximation of the enthalpy of fusion for Pu-rich compositions was calculated using Richard's law [27,28] as a first approximation.

3. Results

Fig. 2 shows, as an example, the heating/cooling cycles performed on a MOX25 specimen. Three high-power pulses were performed in each cycle, separated by longer dwelling periods at an intermediate temperature, around 1500 K. As explained above, the duration of the high-power pulses was increased from one cycle to the other. The corresponding thermograms changed accordingly. In Fig. 2, the three thermograms recorded in each heating-cooling cycle overlap. As already extensively explained in previous work [1–4], a melting inflection is seldom and hardly visible on the thermograms under the current experimental conditions, due to the strongly out-of-equilibrium surface heating produced by the intense laser beam. The melting temperature could only be estimated during heating thanks to the appearance of vibrations in the RLS. Instead, clear thermal arrests/inflections are detectable in the cooling stage of each thermogram overcoming the melting temperature.

One can notice that: (1) Thermograms belonging to the same cycle are generally very well reproducible; the slight change in

the heating rate mostly observed in the first cycle can be attributed to the formation and gradual stabilisation and healing of internal cracks in the material, affecting its thermal conduction; (2) Independently of the different thermogram features, the melting/freezing temperatures observed with the help of RLS and thermal arrests remain the same from a cycle to the other, within the experimental uncertainty.

These remarks are paramount because they show that: (1) The current experimental approach preserves the sample's mechanical stability over numerous heating–cooling cycles beyond melting; (2) Potential segregation effects, linked to non-congruent melting and vaporisation, have no detectable influence on the reproducibility of the current phase transition temperatures.

Fig. 3 displays a clear evolution of the melting onset/solidification arrest temperature with composition. Such solidification arrest occurs at lowest temperatures the interval $0.4 < x(\text{PuO}_2) < 0.7$.

The melting of both pure UO_2 and PuO_2 has been re-investigated with the current approach, too, yielding (3126 ± 55) K and (3050 ± 59) K, respectively. Both values agree, within the reported uncertainties, with those established in the recent literature [2,5]. The uncertainties reported here are larger than those reported in the quoted literature, because here a 2- k coverage factor has been chosen for the statistics (95% confidence bands) instead than 1- k (67% confidence bands). They are moreover consistent with the trend displayed by the melting/solidification points of intermediate compositions.

Table 1 summarises the melting/solidification points observed in the different (U, Pu) O_2 samples investigated in this work.

4. Discussion

4.1. On the melting/solidification processes in pure and mixed compounds

The current melting point of uranium dioxide is slightly lower than the one reported in [2], whereas the melting point of PuO_2 is 33 K higher than the value proposed by De Bruycker et al. [3]. In both cases the differences are largely contained in the experimental error bands, still they can be explained. In fact, here UO_2 was investigated in an external inert gas pressure (0.3 MPa) close to atmospheric, whilst in [2] the value 3147 K was extrapolated from data recorded at high pressure (1 MPa and more), where the melting behaviour was less likely to be affected (lowered) by vaporisation. In the case of PuO_2 the current multiple-pulse laser

heating/cooling cycle approach ensured a better mechanical stability compared with the single shots performed by De Bruycker et al. [3]. A noticeable point is that even in these pure compounds, where the melting/freezing transition is supposed to occur without any compositional change, i.e., congruently, the solidification arrest has a more complex shape than just the expected freezing plateau. Compared to earlier thermograms measured on the same compounds [2,3], this effect is due here to the fact that the sample cools naturally, without any “laser conditioning” of the high cooling speed. On one hand this precaution rules out any uncontrollable effect, on the observed solidification temperature, of the simultaneous presence of the solidification enthalpy release and the heating laser. On the other hand, the high “natural” cooling rate (not laser-conditioned), combined with the relatively poor thermal conductivity of uranium and plutonium dioxides, produces rather large thermal gradients at the periphery of the molten pool, especially during solidification. Consequently, the current phase transition dynamics become rather complex. The aforementioned Phase-Field simulations of the present laser heating experiments help to shed some light on the phenomena involved. Solidification occurs in the cooling liquid pool (which generally extends from the sample surface for a few tens μm into the bulk) starting from preferential nucleation sites, namely the pool bottom and its boundaries on the surface (cf. [2]). The solid front then proceeds towards the centre of the molten zone, where thermal equilibrium conditions are produced during the experiment and where temperature is measured in the pyrometers' focal spot (cf. [25]). However, under these conditions the release of the solidification enthalpy and its diffusion through the coexisting solid and liquid phases is rather complex and difficult to predict. In addition, actinide diffusion is comparatively slow, especially in the solid [29–33]. This makes it difficult to clearly distinguish between a liquidus point (the temperature at which the first solid germ, with a changed composition, appears in the cooling liquid) and a solidus point (the temperature at which the last drop of cooling liquid becomes solid, with the initial composition). The occurrence of a solidus and a liquidus with different compositions implies in fact that the composition change is supported by a molecular diffusion faster than the cooling rate of the system. Such phenomena, already studied in earlier literature [34], can explain why segregation effects are very limited in the samples investigated here.

As a result, the rather complex features often displayed by the current experimental thermal arrests can be attributed to the solidus/liquidus behaviour typical of non-congruent melting/freezing transitions only for compositions whose solidus and liquidus points are sufficiently far apart in temperature (order of a hundred K at least). In the other cases, only a melting/freezing temperature range can be defined based on the current experimental results. Such a temperature range can be defined by combining the RLS analysis on heating and the thermal arrest analysis on cooling. It can be seen in Fig. 3 that the two sets of melting/freezing points are in fair agreement, although RLS melting points are systematically slightly higher. This effect is probably due to the presence of parasite reflections of the heating laser into the pyrometers, and can therefore be included in the uncertainty bands as a systematic error of the technique.

Fig. 4 reports, as an example, the comparison between a Phase-Field simulation and the corresponding experimental thermogram recorded on a $(\text{U}_{0.75}\text{Pu}_{0.25})\text{O}_2$ sample. Despite some differences visible especially at the highest temperatures, where vaporisation and liquid instability leading to additional thermal losses are most difficult to model, the simulation permits a direct interpretation of some features of the empirical thermogram.

The dashed curve represents the PuO_2 molar fraction on the sample surface. It shows that, following the UO_2 – PuO_2 phase boundaries, rather well established in this compositional range

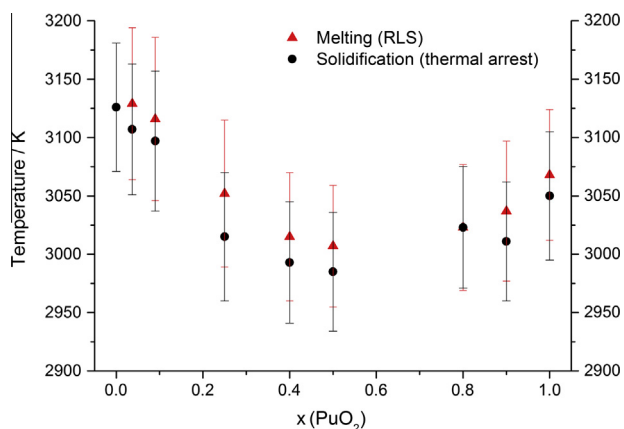


Fig. 3. The melting/solidification temperatures observed in the present work by RLS and thermal arrest analyses on different MOX samples. Vertical uncertainty bands combine the intrinsic instrumental uncertainty (pyrometer calibration, sample emissivity, transmittance of the optical system) with the experimental data spread.

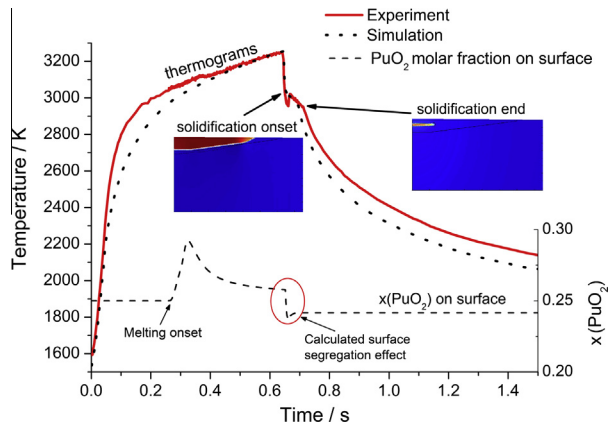


Fig. 4. Experimental (red curve) and Phase-Field calculated (black curve) thermograms of a $(U_{0.75}Pu_{0.25})O_2$ sample laser heated beyond melting. Green curve: PuO_2 concentration on the surface. In the insets: cross section of a sample from centre to rim. The red zone corresponds to the liquid phase with its free energy difference with respect to the solid phase (blue zone). (For interpretation of the references to colour in this figure legend, the reader is referred to the web version of this article.)

(see Section 4.3 below), the newly formed liquid surface is initially enriched in plutonium dioxide. Subsequently, due to fast diffusion in the liquid phase, the initial sample composition ($x(PuO_2) = 0.25$) tends to be rapidly restored. It is however clear, from the simulation, that the fast cooling occurring after the end of the laser pulse leads to onset of solidification before the initial composition is fully recovered in the liquid. A surface solid crust forms then upon freezing before the total liquid mass has crystallised (see insets in Fig. 4). The double inflection during cooling in this case corresponds to the solidification onset on the sample surface (first inflection) and to the disappearance of the last liquid inside the material (second inflection). The highest recalescence temperature represents the solidification point of a composition very close to the initial one (approximately ± 0.01 on $x(PuO_2)$ in the current example), except for small segregation effects. These latter have been studied also experimentally in the present research, by post-melting material characterisation.

4.2. Pre- and post-melting materials characterisation

Pre- and post-melting material characterisation was carried out by XRD, XANES, and Raman Spectroscopy. In particular, the latter technique has been shown to be quick and effective for a rapid local analysis of the sample composition. For this purpose, the Raman active T_{2g} mode typical of fcc fluorite-structured dioxides (symmetry group: $Fm\bar{3}m$) [35] has been taken as a vibrational footprint for the different compounds. This Raman peak is well established to occur at $(445 \pm 1) \text{ cm}^{-1}$ in pure UO_2 and $(478 \pm 1) \text{ cm}^{-1}$ in pure PuO_2 [36]. Comparing the T_{2g} peak position in the molten and unmolten material yielded information on the possible occurrence of local segregation following the quick melting/freezing process (Fig. 5). It should be noted that for PuO_2 contents lower than 10 mol%, the Raman spectra revealed the formation of higher oxides (mostly U_4O_9 and U_3O_8) [37,38] on the sample surface. Fluorescence induced by such oxides hindered the T_{2g} peak analysis in MOX3.7 and MOX9, explaining the larger error band and the somewhat strange trend observed in Fig. 5 for these compositions. Only in the compositions $x(PuO_2) = 0.25$ and $x(PuO_2) = 0.5$, a non-negligible difference between fresh and melted material has been observed, attributable to such segregation effects. One can clearly see an evolution of the T_{2g} position between the pure dioxides. On the other hand, a deeper analysis of the vibrational behaviour and Raman cross-section of the investigated materials would be

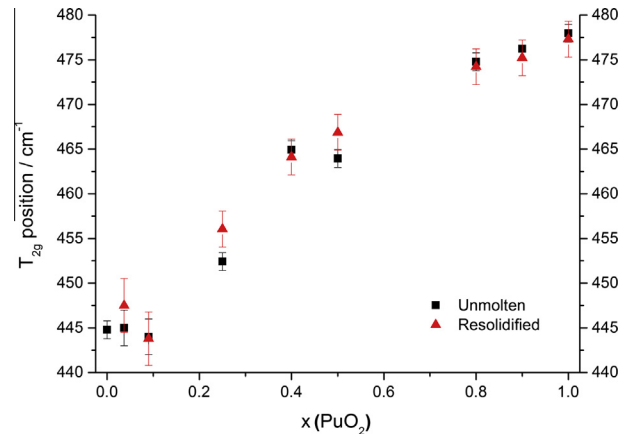


Fig. 5. T_{2g} Raman peak positions of re-solidified (red triangles) and unmolten (black squares) mixed UO_2 – PuO_2 samples. (For interpretation of the references to colour in this figure legend, the reader is referred to the web version of this article.)

needed in order to define a physically meaningful analytical dependence of the peak position on composition (cf. [39]).

XRD characterisation showed that no new phases (such as M_2O_3 , M_4O_9 or M_3O_8 , where $M = U, Pu$) were formed following the fast melting/freezing process, but the original fcc $Fm\bar{3}m$ structure was maintained with the same lattice parameter (within the experimental uncertainty).

The lattice parameters obtained for the different $x(PuO_2)$ by Rietveld analysis of the experimental XRD patterns are shown in Fig. 6.

Slight but obvious deviations from Vegard's law in different intermediate compositions can be attributed to three main reasons: uncertainty in the initially assumed composition of the starting material, segregation or a shift in the oxygen-to-metal (O/M) molar ratio during the melting process. In principle, it is not possible to distinguish a UO_2/PuO_2 composition shift from a shift in O/M through lattice parameter analysis only. However, from the chemical characterisation performed on the current samples before laser irradiation, the $x(PuO_2)$ composition can be assumed to be affected by an uncertainty of ± 0.02 . Since such an uncertainty would justify only very small shifts from Vegard's law, the observed positive variations of the lattice parameter can be safely attributed to

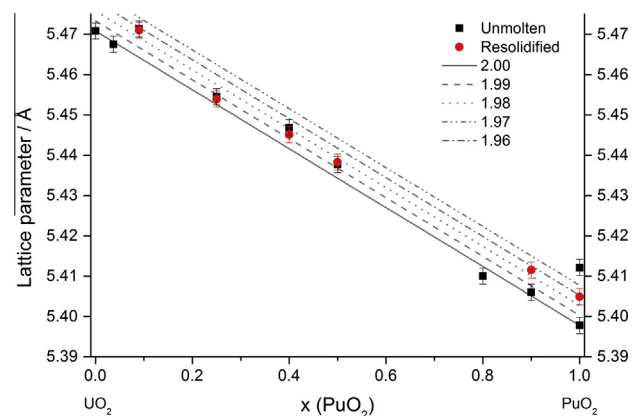


Fig. 6. The lattice parameters obtained by Rietveld analysis of the experimental X-ray diffractograms for the different $x(PuO_2)$ compositions investigated in this work. The black straight solid line represents Vegard's law for an oxygen-to-metal (O/M) ratio = 2.00. Parallel straight lines correspond to different O/M ratios based on data reported in [11]. Three different sample batches have been analysed of pure plutonium oxide. Two have a different age, and the third (labelled " PuO_{2-x} ") is hypo-stoichiometric in oxygen with $O/M = 1.88 \pm 0.07$.

deviations of the oxygen-to-metal molar ratio from the 2.00 exact stoichiometry. For this reason, Fig. 6 also reports straight lines parallel to Vegard's law curve for different O/M ratios, based on data reported in the literature for non-stoichiometric uranium–plutonium mixed dioxides [11]. It can thus be appreciated, from the XRD analysis, that the current samples are mostly slightly hypostoichiometric in oxygen. While the samples with low PuO₂ content do not show any clear difference between the melted/refrozen and the original material, a clear difference is visible only in the mixed composition richest in PuO₂ (MOX90). Because Raman spectroscopy ensured that no relevant uranium dioxide–plutonium dioxide segregation occurred in MOX90 during the laser heating/cooling cycles (cf. Fig. 5), it must be concluded that non-negligible oxygen losses increasing the O/M ratio took place for this composition, probably fostered by the high plutonium content. This point should be further investigated in future research, also bearing in

mind that in the present research oxidation state analysis based on X-ray absorption spectroscopy has been applied only to samples with lower plutonium dioxide contents, considered to be more essential for the nuclear fuel safety. It is worth pointing out here that no such difference in the lattice parameter was noticed in pure PuO₂ before and after laser melting. However, it can be noted in Fig. 6 that different samples of pure PuO₂ present slightly different lattice parameters, too. The current PuO₂ samples differ by age (by a few years), so it is possible that the difference in their lattice parameters corresponds to slight oxygen losses and/or self-radiation damage over storage time. However, no related effect has been observed on the melting behaviour of these pure plutonium dioxide samples.

In conclusion it is clear, from the XRD characterisation, that oxygen behaviour in the mixed oxides, which is directly linked to the oxidation states of U and Pu, constitutes another paramount

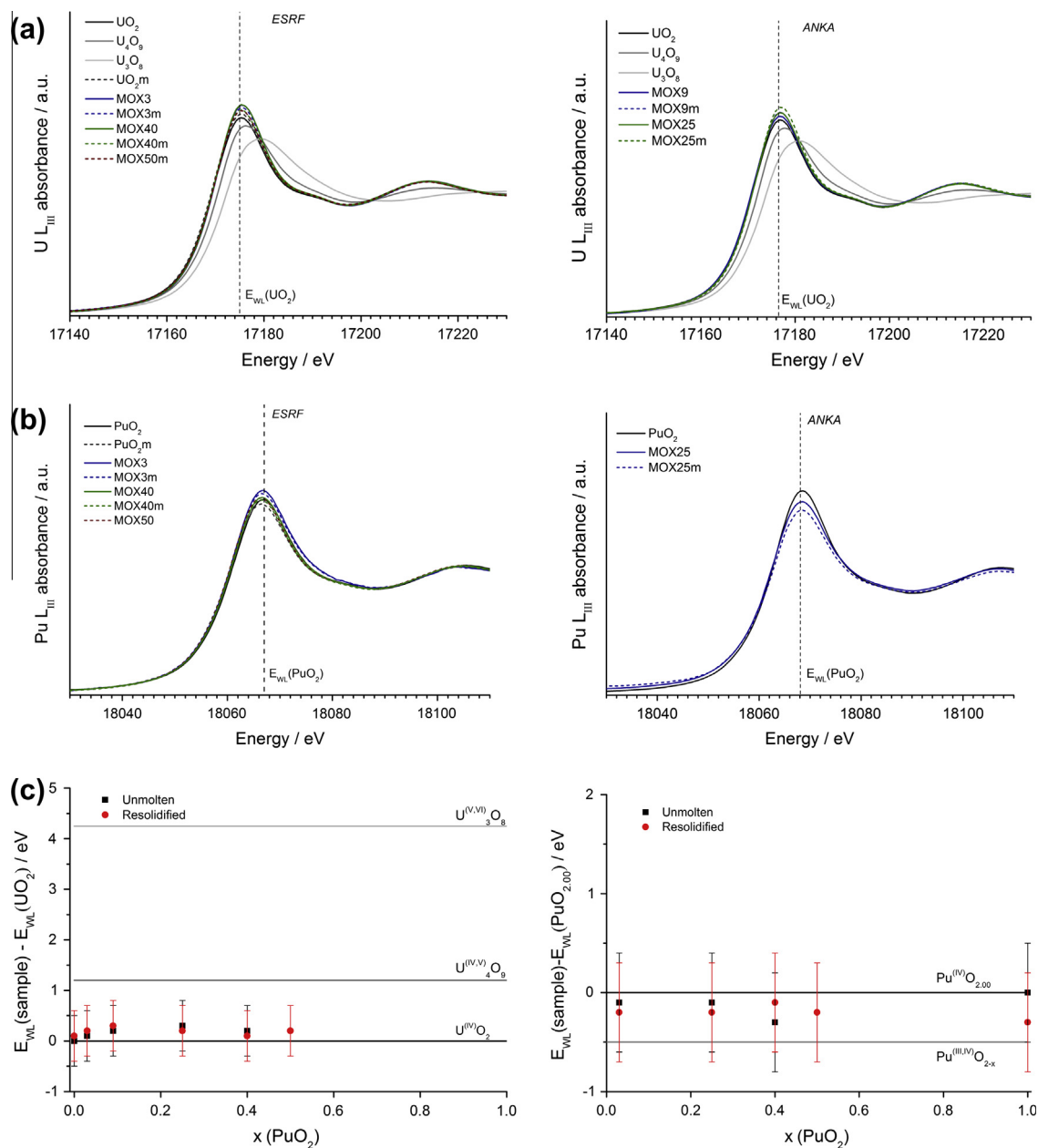


Fig. 7. XANES spectra of the current MOX samples: (a) U L_{III} XANES spectra collected at ESRF (left) and ANKA (right), (b) Pu L_{III} XANES spectra collected at ESRF (left) and ANKA (right), (c) Shift of the U L_{III} and Pu L_{III} white line positions of the MOX samples compared to the UO₂ (left) and PuO₂ (right) white line as a function of the PuO₂ content.

aspect of the fast heating cycles. If both uranium and plutonium should exist in the (IV) oxidation state in the ideal dioxides and their solid solution, a disproportionation can occur, where uranium tends to be oxidised to the (V) or even (VI) states, whereas plutonium tends to be reduced to Pu(III). Moreover, at high temperature non-congruent vaporisation might occur. Such behaviour would have implications on the phase boundaries, which should therefore be considered not in the merely pseudo-binary system $\text{UO}_2\text{–PuO}_2$, but rather in the whole U–Pu–O ternary [5].

A first characterisation of the oxygen behaviour both in fresh and laser irradiated (U, Pu) O_2 samples has been performed with the help of XANES experiments.

XANES results at the U and Pu L_{III} edges in samples with $0 \leq x(\text{PuO}_2) \leq 0.5$, presented in Fig. 7 and Table 2, show that, for a given Pu content, the white lines of the melted and unmelted samples are very similar, indicating that the laser irradiation does not affect significantly the oxygen/metal stoichiometry. In addition, both U and Pu white lines of the MOX samples are well aligned with the UO_2 and PuO_2 reference compounds, which indicates that both U and Pu mostly remain in their tetravalent oxidation states [20] before and after laser irradiation. The O/M ratios of the melted and unmelted MOX samples remain therefore very close to 2.00.

However, slight shifts of 0.1 (5) eV–0.3 (5) eV of the U L_{III} WL and of 0.1 (5) eV–0.3 (5) eV of the Pu L_{III} WL were observed toward higher and lower energies, respectively (cf. Fig. 7a–c and Table 2), both in molten and unmolten MOX samples. Considering the resolution uncertainty, a minor oxidation of the U(IV) to U(V) or U(VI) as well as a minor reduction of Pu(IV) to Pu(III) cannot be totally discarded. Regarding an hypothetical U oxidation in the mixed oxide samples, the oxidation of U(IV) to uranyl U(V) or U(VI) seems quite unlikely as no shoulder located 15 eV after the WL, specific feature or uranyl U(V)/U(VI), was obviously detected on the XANES and HR-XANES spectra [18] (see Figs. 7 and 8). Therefore, we assume that if the shift of the UL_3 WL can be considered as significant with respect to the reported experimental uncertainty, U(IV) in the MOX samples is slightly oxidized to the U(V) uranate type of bonding. This interpretation is consistent with the fact that the experimental HRXANES spectrum of the MOX9 resembles more closely the one of UO_2 and U(IV/V) $_4\text{O}_9$ than the U(IV/VI) $_3\text{O}_8$ reference spectra (Fig. 8). The co-existence of small fractions of U(V) and Pu(III) could be possible as the presence of U(V) compensating for a trivalent cation has already been evidenced in similar fluorite solid solutions [19,40]. If this were the case, the exact O/M = 2.00 stoichiometry would be still at the instrumental uncertainty limit (± 0.03).

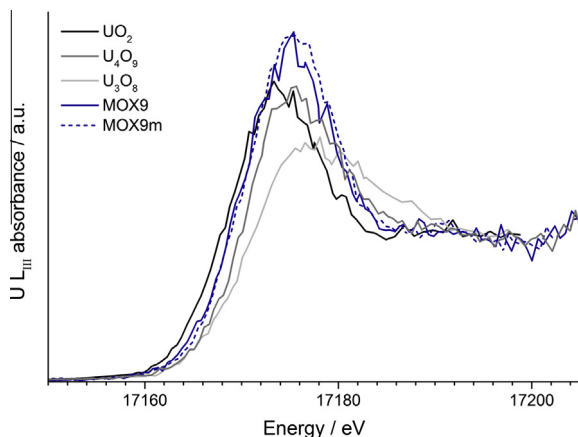


Fig. 8. HR-XANES spectra of MOX9 samples at the U L_{III} edge.

It is important to observe that U(V) and Pu(III) would already be present in the starting unmolten materials. This is a possible consequence of the high-temperature annealing to which samples were subjected prior to the laser heating in order to stabilise the O/M molar ratio at a value as close as possible to 2.00 [4]. This observation might surprise, as the current urania-rich samples have been stored and laser-heated always under an inert atmosphere (nitrogen and pressurised argon, respectively). However, it shows how sensitive to the formation of oxygen defects the current materials can be. This is also one of the crucial points concerning the nuclear fuel's chemical stability [41]. In addition, one cannot exclude the occurrence of reversible deviations from the O/M = 2.00 stoichiometry at very high temperature, where the dioxide is subject to strongly non-congruent vaporisation [5]. This last point is important for predicting the real nuclear fuel behaviour. It is in fact well known [41] that the fuel O/M can change considerably from the stoichiometric 2.00 value as a function of the temperature distribution during in-pile operation.

According to the present Raman, XRD and XANES analyses, very little segregation or oxygen losses are observable in the mixed uranium dioxide–plutonium dioxide samples after laser heating beyond melting, particularly for $x(\text{PuO}_2) \leq 0.5$. This is due to the fact that liquid/solid/gas phase boundaries are probably rather close together in this part of the U–Pu–O system, and to the rapidity of the current heating/cooling processes (cf. [34]). Accordingly, the uncertainty relative to the resulting experimental data points reported in Fig. 3 are representative of the temperature range across which the liquid/solid transition occurs at each composition, and take into account also difficulties in locating the exact liquidus and solidus points, as mentioned before. Possibly, more significant shifts in the O/M or even in the UO_2/PuO_2 ratio would have been observed with slower heating/cooling rates.

4.3. Comparison with CALPHAD optimised phase boundaries

In order to shed some light on the way such deviations might shift the melting/solidification data points reported in Fig. 3, these current experimental results are compared in Fig. 9a–d with previous data, and the phase diagram optimisation performed by Guéneau et al. with the CALPHAD approach [5].

The agreement between the current and previous furnace-heating data is obviously good in the UO_2 -rich part of the phase diagram, where the oxygen potential is the lowest.

On the other hand, it is confirmed that the solid/liquid phase boundaries should be placed at temperatures higher than those measured with traditional heating methods in samples with higher PuO_2 concentrations. This confirms the CALPHAD prediction plotted in Fig. 9, that a minimum melting point should exist in the $\text{UO}_2\text{–PuO}_2$ system, at a composition between $x(\text{PuO}_2) = 0.4$ and $x(\text{PuO}_2) = 0.7$. By considering current and previous data, such minimum melting point is probably located between 2900 K and 3000 K. The large uncertainty still affecting its exact value is certainly linked to the O/M molar ratio stability at very high temperature.

The comparison of experimental data and CALPHAD phase boundary optimisation is shown in Fig. 9 in four transversal sections of the ternary U–Pu–O phase diagram: $\text{UO}_2\text{–PuO}_2$ (a), $\text{UO}_{2.03}\text{–PuO}_2$ (b), $\text{UO}_2\text{–PuO}_{1.96}$ (c) and $\text{UO}_{1.98}\text{–PuO}_{1.96}$ (d). These compositions have been selected in order to compare experimental results with different combination of oxygen/metal (O/M) molar ratios across the phase diagram. They are indicative of the four most likely situations: perfect stoichiometry (a), partial hyper-stoichiometry (b), partial hypo-stoichiometry (c) and complete hypo-stoichiometry (d). It can be noticed that, consistently with published calculations [5], a stable gas phase is foreseen to be present at the equilibrium in the PuO_2 -rich part of each section, unless this

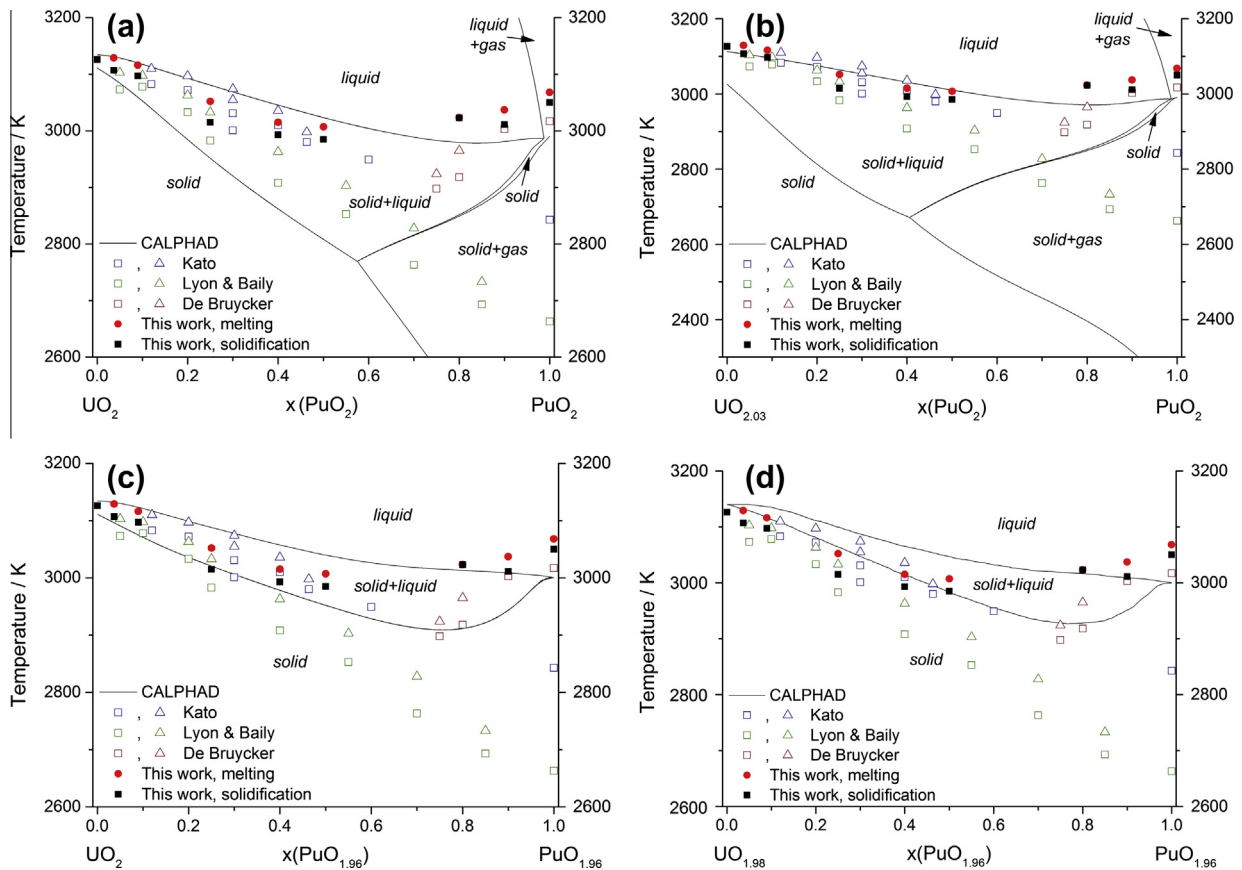


Fig. 9. The current (black squares and red circles) and literature experimental data points (solidus as squares and liquidus as triangles are taken from [4,6,7]) compared with CALPHAD optimised phase boundaries (black dashed curves after [5]): (a) In the pseudo-binary UO_2 – PuO_2 phase diagram, (b) In the “skew” $\text{UO}_{2.03}$ – PuO_2 section of the U–Pu–O ternary system, (c) In the “skew” UO_2 – $\text{PuO}_{1.96}$ section, (d) In the “skew” $\text{UO}_{1.98}$ – $\text{PuO}_{1.96}$ section. (For interpretation of the references to colour in this figure legend, the reader is referred to the web version of this article.)

is sufficiently hypo-stoichiometric as to stabilise the condensed phase (Fig. 9c and d). Independently, the qualitative agreement between the current experimental data and the CALPHAD phase boundaries seems to be acceptable in the four cases.

It is therefore clear, from the current investigation and CALPHAD optimisation, that oxygen equilibria do play a role in these phase boundaries and all the experimental data points (both current and earlier) should be considered with uncertainty bars also in the sense of the O/M molar ratio (perpendicularly to the UO_2 – PuO_2 plane in the ternary phase diagram). Further research is being carried out in order to better define such additional uncertainty bands.

On the other hand, the effect of these oxygen equilibria affects only to a limited extent the qualitative trend of the solidus–liquidus surfaces in the ternary U–Pu–O system in the vicinity of the UO_2 – PuO_2 solid solution. In fact, Fig. 9a–d together with the current Raman, XRD and XANES results show that the temperature range within which the melting/solidification transition has been measured in this work is well indicative of the solid/liquid equilibria in the uranium dioxide–plutonium dioxide system independently of small variations of the O/M ratio and uncertainties.

5. Conclusions

In order to complement recent studies of the melting behaviour of pure plutonium dioxide and (U, Pu) O_2 samples with high-Pu O_2 contents, new results have been obtained on the same material system at JRC-ITU by fast quasi-containerless laser heating. They confirm earlier furnace heating data in the uranium-dioxide rich

part of the phase diagram, and more recent laser-heating data in the plutonium-dioxide side of the system. They suggest that a minimum melting point must exist in the UO_2 – PuO_2 system, at a composition between $x(\text{PuO}_2) = 0.4$ and $x(\text{PuO}_2) = 0.7$ and $2900 \text{ K} \leq T \leq 3000 \text{ K}$. Taking into account that, especially at high temperature, oxygen defects and O/M molar ratio variations have an effect on the reported phase boundary uncertainties, the current results should be projected in the ternary U–Pu–O system. Further research is on-going, aiming at a better definition of uncertainty bands in the O/M molar ratio both at room and high temperature. However, these uncertainty bands are not expected to significantly affect the qualitative trend of the current solid–liquid phase boundaries.

The current results have important implications not only in terms of fundamental materials understanding, but also for the comprehension of the nuclear fuel behaviour in case of an accident during which the temperature would exceed the melting limit. In particular, the new insight provided by the current work will help to clarify and reduce the margin to melting uncertainties.

Acknowledgements

The Authors are indebted to J. Somers, D. Staicu, T. Wiss and Z. Talip (JRC-ITU) for providing the (U, Pu) O_2 and U_4O_9 samples, as well as for their scientific advice. They wish to convey their gratitude to P. Raison, R. Eloirdi, T. Wiss, A. Janssen, G. Pagliosa, D. Bouexière and M. Sierig (JRC-ITU) for their precious help in the sample characterisation, as well as N. Fink and C. Marquardt (KIT-INE), P. Colomp and A. Scheinost (ESRF) for their help in organising the XAS characterisation. This latter has partially been financed by

the European-FP7 TALISMAN project and the Helmholtz Association of German Research Centres (VH-NG-734). The Synchrotron Light Sources ANKA and ESRF are acknowledged for provision of instruments at their beamlines.

Appendix A. Supplementary material

Supplementary data associated with this article can be found, in the online version, at <http://dx.doi.org/10.1016/j.jnucmat.2014.02.029>.

References

- [1] D. Manara, M. Sheindlin, W. Heinz, C. Ronchi, *Rev. Sci. Instrum.* 79 (2008) 113901.
- [2] D. Manara, C. Ronchi, M. Sheindlin, M. Lewis, M. Brykin, *J. Nucl. Mater.* 342 (2005) 148.
- [3] F. De Bruycker, K. Boboridis, D. Manara, P. Poeml, M. Rini, R.J.M. Konings, *Mater. Today* 13–11 (2010) 52–55.
- [4] F. De Bruycker, K. Boboridis, R.J.M. Konings, M. Rini, R. Eloirdi, C. Guéneau, N. Dupin, D. Manara, *J. Nucl. Mater.* 419 (2011) 186.
- [5] C. Guéneau, N. Dupin, B. Sundman, C. Martial, J.-C. Dumas, S. Gossé, S. Chatain, F. De Bruycker, D. Manara, R.J.M. Konings, *J. Nucl. Mater.* 419 (2011) 145.
- [6] W.L. Lyon, W.E. Baily, *J. Nucl. Mater.* 22 (1967) 322–339.
- [7] M. Kato, K. Morimoto, H. Sugata, K. Konashi, M. Kashimura, T. Abe, *J. Nucl. Mater.* 373 (2008) 237–245.
- [8] T. Hiroshawa, I. Sato, *J. Nucl. Mater.* 418 (2011) 207.
- [9] D. Manara, R. Böhler, K. Boboridis, L. Capriotti, A. Quaini, L. Luzzi, F. De Bruycker, C. Guéneau, N. Dupin, R.J.M. Konings, *Proc. Chem.* 7 (2012) 505.
- [10] H. Kinoshita, D. Setoyama, Y. Saito, M. Hirota, K. Kurosaki, M. Uno, S. Yamanaka, *J. Chem. Thermodyn.* 35 (2003) 719.
- [11] C. Guéneau, A. Chartier, L.V. Brutzel, *Thermodynamic and Thermophysical Properties of the Actinide Oxides*, in: R.J.M. Konings (Ed.), *Compre. Nucl. Mater.*, first ed., Elsevier, Amsterdam, 2012.
- [12] L. Petit, A. Svane, Z. Szotek, W.M. Temmerman, G.M. Stocks, *Phys. Rev. B* 81 (2010) 045108.
- [13] J.H. Parker Jr., D.W. Feldman, M. Ashkin, *Phys. Rev.* 155 (1967) 712.
- [14] T. Vitova, K.O. Kvashnina, G. Nocton, G. Sukharina, M.A. Denecke, S.M. Butorin, M. Mazzanti, R. Caciuffo, A. Soldatov, T. Behrends, H. Geckeis, *Phys. Rev. B* 82 (2010) 235118.
- [15] J. Rothe, S. Butorin, K. Dardenne, M.A. Denecke, B. Kienzler, M. Löble, V. Metz, A. Seibert, M. Steppert, T. Vitova, C. Walther, H. Geckeis, *Rev. Sci. Instrum.* 83 (2012) 043105.
- [16] W. Matz, N. Schell, G. Bernhard, F. Prokert, T. Reich, J. Claußner, W. Oehme, R. Schlenk, S. Diemel, H. Funke, F. Eichhorn, M. Betzl, D. Pröhl, U. Strauch, G. Hüttig, H. Krug, W. Neumann, V. Brendler, P. Reichel, M.A. Denecke, H. Nitsche, *J. Synchrotron Rad.* 6 (1999) 1076.
- [17] B. Ravel, M. Newville, *J. Synchrotron Radiat.* 12 (2005) 537.
- [18] S.D. Conradson, D. Manara, F. Wastin, D.L. Clark, G.H. Lander, L.A. Morales, J. Rebizant, V.V. Rondinella, *Inorg. Chem.* 43 (2004) 6922.
- [19] D. Prieur, P.M. Martin, A. Jankowiak, E. Gavilan, A.C. Scheinost, N. Herlet, P. Dehaut, P. Blanchart, *Inorg. Chem.* 50 (2011) 12437.
- [20] S.D. Conradson, K.D. Abney, B.D. Begg, E.D. Brady, D.L. Clark, C. den Auwer, M. Ding, P.K. Dorhout, F.J. Espinosa-Faller, P.L. Gordon, R.G. Haire, N.J. Hess, R.F. Hess, D.W. Keogh, G.H. Lander, A.J. Lupinetti, L.A. Morales, M.P. Neu, P.D. Palmer, P. Paviet-Hartmann, S.D. Reilly, W.H. Runde, C.D. Tait, D.K. Veirs, F. Wastin, *Inorg. Chem.* 43 (2004) 116.
- [21] P. Martin, S. Grandjean, C. Valot, G. Carlot, M. Ripert, P. Blanc, C. Hennig, *J. Alloys Compd.* 444–445 (2007) 410–414.
- [22] R.C. Belin, P.M. Martin, J. Lechelle, M. Reynaud, A.C. Scheinost, *Inorg. Chem.* 52 (2013) 2966.
- [23] S. Grandjean, B. Arab-Chapelet, A.C. Robisson, F. Abraham, P. Martin, J.-P. Dancausse, *J. Nucl. Mater.* 385 (2009) 204.
- [24] M.J. Welland, W.T. Thompson, B. Lewis, D. Manara, *J. Nucl. Mater.* 385 (2009) 358–363.
- [25] R. Böhler, M.J. Welland, F. De Bruycker, K. Boboridis, A. Janssen, R. Eloirdi, R.J.M. Konings, D. Manara, *J. Appl. Phys.* 111 (2012) 113501.
- [26] J.K. Finck, *J. Nucl. Mater.* 279 (2000) 1.
- [27] P. Papon, J. Leblond, P.H.E. Meijer, *The Physics of Phase Transitions*, second ed., Springer, Berlin, 2002.
- [28] L.F. Epstein, *J. Nucl. Mater.* 22 (1967) 340.
- [29] Q. Yin, S.Y. Savrasov, *Phys. Rev. Lett.* 100 (2008) 225504.
- [30] M. Bober, G. Schumacher, *Adv. Nucl. Sci. Technol.* 7 (1973) 121.
- [31] H.J. Matzke, *J. Nucl. Mater.* 114 (1983) 121.
- [32] M.J. Welland, *Fast reactor fuel restructuring*, in: R. Konings (Ed.), *Comprehensive Nuclear Materials*, Elsevier Science, 2012. Chapter 73.
- [33] V. Di Marcello, A. Schubert, J. van de Laar, P. Van Uffelen, *Nucl. Eng. Des.* 248 (2012) 149.
- [34] M.J. Aziz, T. Kaplan, *Acta Metall.* 36 (1988) 2335.
- [35] V.G. Keramidis, W.B. White, *J. Chem. Phys.* 59 (1973) 1561.
- [36] G.M. Begun, R.G. Haire, W.R. Wilmarth, G.R. Peterson, *J. Less Common Metals* 162 (1990) 129.
- [37] H. Idriss, *Surf. Sci. Reports* 65 (2010) 67.
- [38] L. Desgranges, G. Baldinozzi, P. Simon, G. Guimbretièred, A. Canizares, *J. Raman Spectrosc.* 43 (2012) 455.
- [39] J.-C. Panitz, J.-C. de Mayor, B. Grob, W. Durisch, *J. Alloys Compd.* 303–304 (2000) 340.
- [40] D. Prieur, P. Martin, F. Lebreton, T. Delahaye, D. Banerjee, A.C. Scheinost, A. Jankowiak, *J. Nucl. Mater.* 434 (2013) 7.
- [41] D. Olander, *J. Nucl. Mater.* 389 (2009) 1.